Critical soil moisture detection and water-energy limit shift attribution using satellite-based water and carbon fluxes over China

Yi Liu[1], Jingfeng Xiao[2], Xing Li[3], Yue Li[4]

[1]School of Civil Engineering and Architecture, Guangxi University, Nanning 530004, China
[2]Earth Systems Research Center, Institute for the Study of Earth, Oceans, and Space, University of New Hampshire, Durham, NH 03824, USA
[3]School of Geography and Planning, Sun Yat-Sen University, Guangzhou 510275, China
[4]Department of Earth Sciences, Indiana University-Purdue University Indianapolis (IUPUI), Indianapolis, IN 46202, USA

Correspondence to: Yi Liu (liuyi.15b@igsnrr.ac.cn)

Abstract. Critical soil moisture (CSM), a tipping point of soil moisture (SM) at which surface fluxes shift from energy- to water-limited regimes, is essential for the vegetation state and corresponding land-atmosphere coupling. However, detecting CSM and attributing water-energy limit shifts to climate and ecosystem variables are challenging as in-situ observations of water, carbon fluxes, and SM are sparse. In this study, CSM was assessed over China in June–September over the period 2001–2018 using two satellite-based methods: the difference between the correlation between SM and evapotranspiration (ET) and the correlation between vapor pressure deficit (VPD) and ET; the covariance between VPD and gross primary production (GPP). ET and GPP products were based on the Penman-Monteith-Leuning (PML) ET and GPP, Global LAnd Surface Satellite (GLASS) ET and GPP, Collocation-Analyzed Multi-source Ensembled Land Evapotranspiration (CAMELE) ET, Surface Energy Balance Algorithm for Land (SEBAL) ET, Two-Leaf light use efficiency model based (TL) GPP, and SIF-based (GOSIF) GPP. At flux sites, ET and GPP products were evaluated by eddy covariance-based measurements; CSM values using two satellite-based methods were assessed by CSM using the soil moisture-evaporative fraction method. Their consistency at site scales demonstrated reliable results and applicability to regional scales. Through intercomparison, the spatial pattern of CSM from multi-source ET and GPP datasets across China was consistent and robust in eastern and southern basins. Generally, CSM decreased from southern to northern regions. Pearl River Basin and Southeastern River Basin displayed a relatively high CSM for clay-rich soils (e.g., 0.39 m^3/m^3 using PML ET and 10 cm depth SM~~),~~) and forests (e.g., 0.~~37~~35 m^3/m^3 using PML ET and 10 cm depth SM). For four soil layers, grassland and clay had higher CSM than SM, making them in water-limited regimes. Thus, western grassland with increased ET was more susceptible to water stress. These findings highlight the variability in CSM and primary determinants of water-energy limit shifts, offering valuable insights into the potential water limitation on ecosystems under comparable SM circumstances.

1 Introduction

Critical soil moisture (CSM) serves as an indicator of shifts in the relationship between water and energy availability (Schwingshackl et al., 2017; Denissen et al., 2020) and is essential in shaping regional climates. Plants adjust their stomatal resistance in response to changes in soil moisture (SM) and vapor pressure deficit (VPD) (Grossiord et al., 2020; Li, F. et al., 2023). Above CSM, there is no alteration in water stress with SM increases (Rodriguez-Iturbe, 2000; Seneviratne et al., 2010; Akbar et al., 2018); plants are primarily controlled by VPD. Warm and dry air above the canopy (Grossiord et al., 2020; Li, X. et al., 2023) leads to a decrease in both the transpiration process as the largest part of evapotranspiration (ET) (Good et al., 2015) and gross primary production (GPP) coupled with the ET process via plant leaf stomata (Gentine et al., 2019; Liu et al., 2020). A decrease in ET, in turn, results in elevated surface temperature and VPD~~)~~ (Gentine et al., 2019) and leads to increased atmospheric aridity on a large spatial scale, thereby intensifying the depletion of SM. Below CSM, surface fluxes are primarily influenced by SM availabilities in conditions of restricted water supply. During this period, a decrease in SM results in a reduction in latent heat flux (LE) and an increase in sensible heat flux (H) (Rodriguez-Iturbe, 2000); the relationship between SM and leaf conductance follows a linear trend (Laio et al., 2001; Porporato et al., 2002). Previous studies have examined land-atmosphere feedback using different metrics and both observation and simulation data (Seneviratne et al., 2006; Koster et al., 2009; Teuling et al., 2009). They found that water and energy limit shifts may be further strengthened by the interaction between the land and atmosphere, particularly when positive feedback mechanisms known as the "dry gets dryer" effect (Seneviratne et al., 2010; Gentine et al., 2019). Over extended temporal periods, this phenomenon may lead to the persistence of arid and high-temperature conditions (Zhang et al., 2020). Consequently, it is necessary to quantify the characteristics of CSM and the influencing environmental factors of water-energy limit shifts.

Traditionally, under the framework based on the ratio of LE to the total of LE and H (Haghighi et al., 2018; Fu et al., 2022b), sparse eddy covariance observations (Feldman et al., 2019; Fu et al., 2022a) pose challenges in adequately capturing comprehensive regional or continental-scale CSM and its variations (Dong et al., 2023; Hsu and Dirmeyer, 2023a). In recent years, the feasibility of conducting large-scale analysis has been enhanced by the growing accessibility of multi-source satellite-based datasets (Liu et al., 2012). Globally, some model-based analyses used the ratio of LE to net radiation (Seneviratne et al., 2010; Schwingshackl et al., 2017), surface temperature diurnal amplitude (Feldman et al., 2019; Fu et al., 2024), and LE (Hsu and Dirmeyer, 2023b; Duan et al., 2023). In addition, the advancement of global remote sensing products technology has facilitated the generation of reliable GPP products (Yuan et al., 2014; Li and Xiao, 2019; Zhang et al., 2019; Bi et al., 2022; He et al., 2022; Li, F. et al., 2023) and ET products (Yao et al., 2013; Yao et al., 2014; Zhang et al., 2019; Cheng et al., 2021; He et al., 2022; Li, C. et al., 2022; Li, F. et al., 2023~~).~~), which are used in CSM studies. Denissen et al. (2020) proposed a new tipping-point metric, the difference between the correlation between SM and ET and the correlation between VPD and ET, to straightforwardly determine CSM at continental scales. Fu et al. (2022a) first demonstrated that the covariance between GPP and VPD indirectly quantifies CSM. The point at which covariance between GPP and VPD transitions from positive to negative during a period of soil drying is denoted as CSM. However, a source of considerable uncertainty when considering only a single data source and estimation approach exists at a large spatial scale. There are significant differences among satellite-based ET and GPP datasets, and CSM varies with different methods, leading to uncertainty as to whether CSM of carbon flux is the same as that of water flux.

Chinese land surface frequently experiences water~~ and ~~-energy limit shifts (Xiao, 2014; Zhu et al., 2023). Diagnosing CSM across various biomes and climatic zones helps to understand water-energy limit regimes determined by distinct flora and soil types (Homaee et al., 2002; Hsu and Dirmeyer, 2023b). The association between water, energy, and flux helps to define water-energy limit shifts. As such, this study uses two innovative metrics and eight satellite-based products to diagnose CSM and water-energy limit shifts across China. The goal of this study is to~~:~~ (1) assess the consistency of different methods in calculating CSM at flux sites; (2) examine CSM variations across land cover types, soil textures, and water resource subregions; and (3) investigate dominant factors from climate and ecosystem variables that influence water-energy limit shifts.

2 Material and methods

2.1 Data

Eddy covariance flux datasets were compared with eight satellite-based ET and GPP in Section 3.1. Then, CSM derived from the relationship between SM and evaporative fraction (EF) was used to evaluate the performance of CSM derived from the covariance and correlation-difference methods in Section 3.2. Layer-wise SM and satellite-based ET and GPP were used for the large-scale detection of CSM. Land cover type, soil texture, and water resource regionalization were all used to examine CSM variations in Section 3.3. SM, ET, GPP, and meteorological data were all used to investigate dominant factors influencing water-energy limit shifts in Section 3.4. All energy, vegetation, and water variables were resampled or combined to 0.1°-8 days resolution. The period, limited by the temporal availability of several data sources, covered 2001–2018.

2.1.1 Evapotranspiration and gross primary production

Figure 1 illustrates locations of 21 flux sites, and Table 1 shows the detailed information on flux sites. Eddy covariance-derived measurements were applied to evaluate the performance of satellite-based ET and GPP. Given the fact that Huazhaizi, Dashalong, Luodi, Arou, Guantao, Huailai, Miyun, and Daxing did not have GPP data, REddyProc website (https://www.bgc-jena.mpg.de/5622399/REddyProc/) was used to calculate GPP. REddyProc imported half-hourly net ecosystem exchange, LE, H, and meteorological measurements to partition net ecosystem exchange into GPP and ecosystem respiration.
Table 2 contains a list of all spatial data sets used in this study. Advances in remote sensing have substantially fostered the development of global ET and GPP products for CSM simulation. Eight satellite-based ET and GPP products are included. Penman-Monteith-Leuning (PML), with a spatiotemporal resolution of 500 m and 1 day during February 2000–December 2020, integrates the stomatal conductance theory to relate ET and GPP processes using the Penman-Monteith-Leuning model (Zhang et al., 2019; He et al., 2022) and applies daily meteorological data, land surface temperature from ERA5, enhanced Whittaker-filtered MODIS LAI, albedo, and emissivity. The interdependency and mutual restrictions between GPP and ET

considerably increase the accuracy of the simulation. Global LAnd Surface Satellite (GLASS) ET, with 0.05° resolution and every 8 days, integrates the MOD16, a revised remote sensing-based Penman-Monteith, the Priestley-Taylor Jet Propulsion Laboratory, a modified satellite-based Priestley-Taylor, and the Semi-Empirical Algorithm of the University of Maryland using the Bayesian model averaging approach (Yao et al., 2013; Yao et al., 2014); GLASS GPP algorithm incorporates effects of atmospheric carbon dioxide content, radiation components, and VPD based on the eddy covariance-light use efficiency model introduced by Yuan et al. (2007). It is founded on two underlying assumptions: the fraction of absorbed photosynthetically active radiation has a linear relationship with the normalized difference vegetation index; constant light use efficiency is governed by either air temperature or soil moisture, depending on which component imposes the greatest limitation.

In addition, Collocation-Analyzed Multi-source Ensembled Land Evapotranspiration (CAMELE) provides long-term (1981–2020) ET, employing ERA5, FLUXCOM, PML, GLDAS, and GLEAM (Li, C. et al., 2022), at 0.1°-8 days and 0.25°-daily resolutions. Surface Energy Balance Algorithm for Land (SEBAL) ET focuses on 1 km-daily resolution during 2001–2018. This product integrates GMAO's meteorological data and NASA's MOD43A1 daily surface albedo, MOD11A1 daily surface temperature, and MOD13 vegetation index (Cheng et al., 2021). Two-Leaf light use efficiency model-based (TL) GPP offers comprehensive worldwide assessments of GPP, shaded GPP, and sunlit GPP at a spatiotemporal resolution of 0.05°-8 days, covering the period from 1992 to 2020. This model applies recent data inputs such as the GLOBMAP LAI, CRUJRA meteorological data, and ESA-CCI land cover information (Bi et al., 2022). Global, Orbiting carbon observatory-2 SIF-based (GOSIF) GPP spans from 2000 to 2020 with 0.05°-8 days resolution. A total of eight SIF-GPP relationships, including both universal and biome-specific formulations, are used to estimate GPP from SIF on a per-pixel basis and examined with and without intercept terms to account for the uncertainty in converting SIF into GPP estimates (Li and Xiao, 2019).

2.1.2 Layer-wise soil moisture and meteorological data

Given the recent availability of state-of-the-art gridded SM in China released by Li, Q. et al. (2022), CSM can now be investigated in the context of the SM state. Gridded SM reaches 100 cm soil depth with 10 cm intervals at 1 km-daily resolution during 2000–2020. It is trained by predictors of ERA5-Land time series, leaf area index (LAI), land cover type, topography, and in-situ observed soil attributes at 1789 stations throughout China, using the robust random forest machine learning technique. Based on the findings of Li, Q. et al. (2022), the product demonstrates notable benefits over both ERA5-Land and SMAP-L4 datasets, especially in terms of a superior quality level compared to the SoMo.ml dataset at soil depths of 10, 20, 80, and 100 cm. Thus, this study utilized SM at these layers.

Yang et al. (2010) and He et al. (2020) put forth a comprehensive dataset for Chinese regional surface meteorological forcing. This dataset encompasses air temperature, air pressure, specific humidity, wind speed, downward shortwave radiation, downward longwave radiation, and precipitation. It is presented in the NetCDF format with a spatiotemporal resolution of 0.1°-3 hours during 1979–2018. The primary input includes Princeton University's Global Land Surface Model Data, GLDAS, GEWEX-SRB radiation, TRMM precipitation, and China Meteorological Administration observations. Data quality control techniques include the elimination of physically implausible values and statistical interpolation using ANU-Spline. This dataset demonstrates precision levels that lie between those of site-based observation and satellite-based estimation, therefore exceeding the accuracy of current international reanalysis datasets. In this study, VPD was computed by specific humidity and air temperature; VPD, air temperature, precipitation, and downward shortwave radiation were employed in the examination of water and energy limitations.

2.1.3 Land cover types, soil textures, and water resource subregions

Land cover types, soil textures, and water resource subregions influence CSM. In this study, land cover types (2020) were created by human visual interpretation relying on Landsat satellite remote sensing images. It utilized a categorization scheme including cropland, forests, grassland, water, ice, urban, and barren. Soil textures were compiled from the 1:1,000,000 soil type map and the second national soil survey. It was expressed as sand, silt, and clay content within each grid cell. Water resource subregions divided by the China Geological Survey included Zhungaer Basin, Pearl River Basin, Yangtze River Basin, Southwestern River Basin, Tarim Basin, Songhua River Basin, Changthang Region, Inner Mongolian Plateau Region, Liaohe River Basin, Yellow River Basin, Huaihe River Basin, Hexi Corridor Region, Haihe River Basin, Southeastern River Basin, and Qaidam Basin. The water resources sub-region was based on the principles of groundwater systems and water cycles and focused on the inherent features of groundwater resources within distinct natural units.

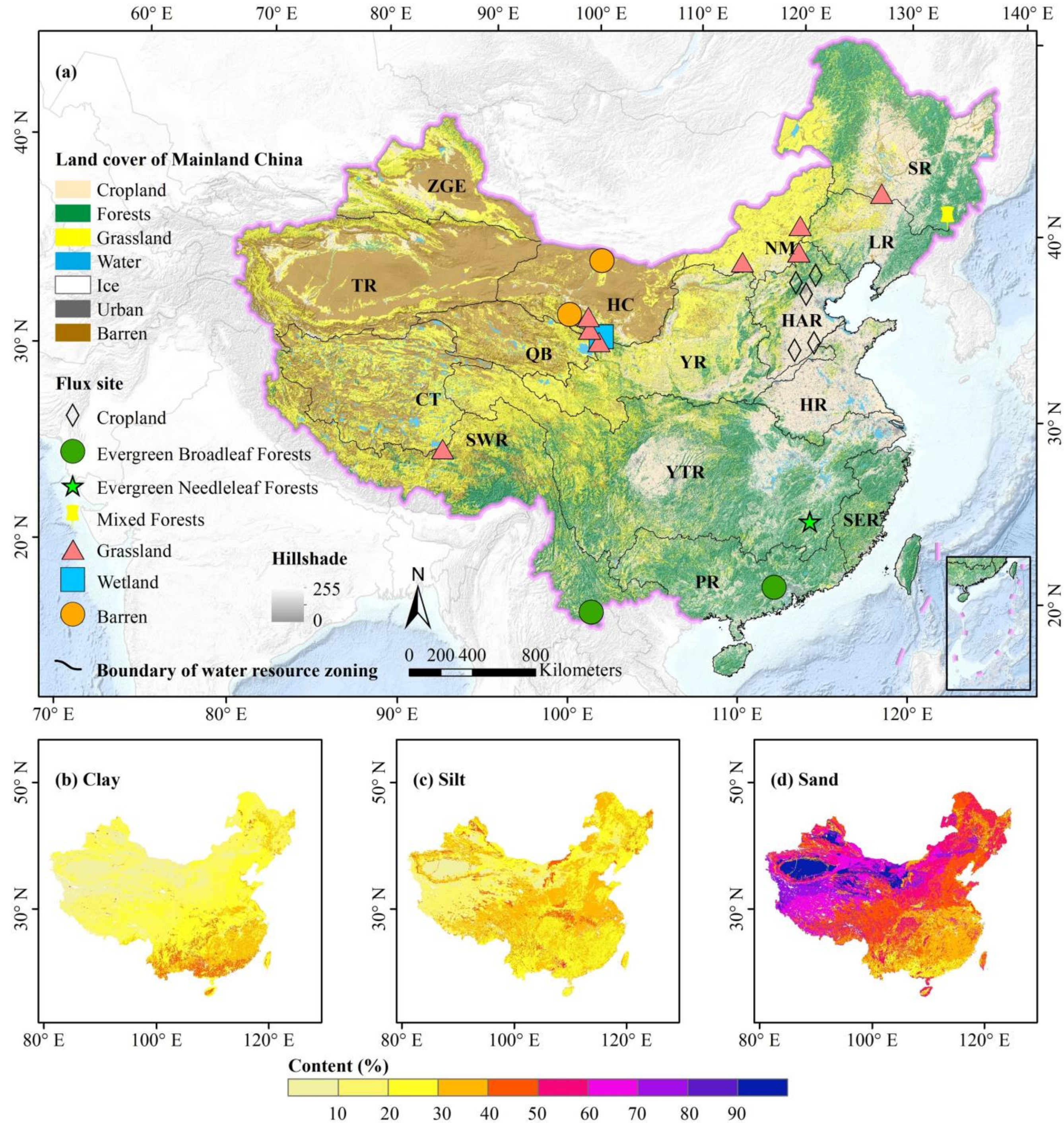

Figure 1: (a) Locations of flux sites, land cover types (2020), and water resource subregions of China. **Distributions of (b) clay, (c) silt, and (d) sand content (1995). ZGE: Zhungaer Basin, PR: Pearl River Basin, YTR: Yangtze River Basin, SWR: Southwestern River Basin, TR: Tarim Basin, SR: Songhua River Basin, CT: Changthang Region, NM: Inner Mongolian Plateau Region, LR:**

Liaohe River Basin, YR: Yellow River Basin, HR: Huaihe River Basin, HC: Hexi Corridor Region, HAR: Haihe River Basin, SER: Southeastern River Basin, QB: Qaidam Basin.

Table 1: Flux site information used in this study.

Site	Land cover types	Latitude	Longitude	Time span	Source
CN-Sw2		41.79	111.89	2011	Fluxnet
CN-Du2		42.04	116.28	2006–2008	Fluxnet
CN-Du3		42.05	116.28	2009–2010	Fluxnet
CN-Cng		44.59	123.51	2007–2010	Fluxnet
Damshung	Grassland	30.49	91.06	2004–2010	Chinaflux
Xilingela		43.53	116.67	2004–2010	Chinaflux
Haibei1		37.37	101.18	2003–2010	Chinaflux
Dashalong		38.84	98.94	2013–2015	TPDC
Arou		38.04	100.46	2013–2015	TPDC
Daxing		39.62	116.43	2008–2010	TPDC
Miyun		40.63	117.32	2008–2009	TPDC
Huailai	Cropland	40.35	115.79	2014–2018	TPDC
Guantao		36.52	115.13	2008–2009	TPDC
Yucheng		36.82	116.57	2003–2010	Chinaflux
Xishuangbanna	Evergreen broadleaf forests	21.92	101.26	2003–2010	Chinaflux
Dinghushan		23.16	112.53	2003–2010	Chinaflux
Qianyanzhou	Evergreen needleleaf forests	26.74	115.05	2003–2010	Chinaflux
Changbaishan	Mixed forests	42.40	128.09	2003–2010	Chinaflux
Haibei2	Wetland	37.66	101.33	2004–2009	Chinaflux
Huazhaizi	barren	38.76	100.32	2013–2015	TPDC
Luodi		41.99	101.13	2014–2015	TPDC

TPDC: National Tibetan Plateau Data Center

Table 2: Spatial gridded data sets used in this study.

Variable	Dataset	Spatial resolution	Temporal resolution	Unit	Time span	Reference
Soil moisture	SMCI1.0	0.1°	day	$0.001 m^3/m^3$	2000–2020	Li, Q. et al. (2022)
	GLASS	0.05°	8-day	W/m^2	2000–2018	Yao et al. (2013, 2014)
Evapotranspiration	PML	500 m	day	0.01mm	2000–2020	Zhang et al. (2019) and He et al. (2022)
	CAMELE	0.1°	8-day	$kg/ m^2 /s$	2001–2019	Li, C. et al. (2022)
	SEBAL	1 km	day	mm	2001–2018	Cheng et al. (2021)
	GLASS	0.05°	8-day		1982–2018	Yuan et al. (2014)
Gross primary production	PML	500 m	day	gC/m^2	2000–2020	Zhang et al. (2019) and He et al. (2022)
	GOSIF	0.05°	8-day		2000–2021	Li and Xiao (2019)
	TL	0.05°	8-day		1992–2020	Bi et al. (2022)
Specific humidity	-	0.1°	3-hour	$kg\ kg^{-1}$	1979–2018	

Air temperature				K		
Downward shortwave radiation				W m^{-2}		Yang et al. (2010) and He et al. (2020)
Precipitation				mm hr^{-1}		
Land cover	-	1 km	-	-	2020	http://www.resdc.cn
Soil texture	-	1 km	-	-	1995	http://www.resdc.cn

2.2 Determination of CSM

CSM, which captures the interconnectedness between SM and EF, derived by the SM and EF method, was used to assess the CSM from ET and GPP on the site scale. There must be both positive and negative metrics from the covariance and correlation-difference methods. For each grid cell and the entire period per year, negative metrics are displayed when SM is less than CSM, and positive metrics are shown when SM is greater than CSM. If there is more than one value where SM shifts between positive and negative metrics, CSM is treated as unidentified.

The data will be taken into account just when the temperature surpasses 10° (Denissen et al., 2020) to avoid the influence of ice and snow, and the covariance between VPD and GPP must exhibit a minimum of 7 covariance values within 9-day moving windows, with a minimum of 15 data (Fu et al., 2022a). Hence, we concentrated on the warm season, June–September, which includes 16 data each year with 9 covariance values within 8-value moving windows. CSM was conducted in each grid cell using satellite-based ET and GPP over the period 2001–2018.

2.2.1 Soil moisture-evaporative fraction method

Investigating the relationship between SM and EF in the dry period can isolate the transition from energy limitation to water limitation (Feldman et al., 2019). If SM is greater than or less than CSM, the relationship between SM and EF appears as a flat line or a positive slope line. A linear-plus-plateau model characterizes the relationship precisely measured by eddy covariance flux towers (Seneviratne et al., 2010; Schwingshackl et al., 2017):

$$\mathrm{EF} = \begin{cases} \mathrm{EF_{max}} + \mathrm{S}(\mathrm{SM} - \mathrm{CSM}), \text{if } \mathrm{SM} < \mathrm{CSM} \\ \mathrm{EF_{max}}, \text{if } \mathrm{SM} \geq \mathrm{CSM} \end{cases}, \tag{1}$$

where EF is the evaporative fraction defined as LE/(LE+H); $\mathrm{EF_{max}}$ represents the maximum EF in the energy-limited stage, and S is the gradient in the water-limited stage. Here, specific estimated CSM was simultaneously estimated by the Monte Carlo method. For a set of optimal parameters, the Nash-Sutcliffe efficiency (Nash and Sutcliffe, 1970) above 0.5 was considered satisfactory (Herman et al., 2018). Thus, only 8 sites, including Xilingela in 2004, Damshung in 2004, CN-Sw2 in 2011, CN-Du2 in 2007, CN-Cng in 2010, Miyun in 2009, Huailai in 2015, and Qianyanzhou in 2010, were chosen for CMS detection. In addition, the Bayesian Information Criterion (BIC) (Schwarz 1978) was used to select the best fit among three-segmented regression candidates (the flat line, the positive slope line, and the linear-plus-plateau). If the flat-line regression or the positive-slope regression outperformed the linear-plus-plateau regression, CSM was considered as not identified.

2.2.2 Covariance method

The covariance method presents a novel method for assessing ecosystem water stress in direct correlation with GPP, as illustrated by Fu et al. (2022a). It serves to quantify CSM over large areas. Positive covariances between VPD and GPP indicate that energy limits GPP. Negative covariances indicate that water limitation has a larger impact on GPP. VPD is determined by the disparity between the saturation vapor pressure (es) and the actual vapor pressure (ea). Bolton (1980) posits that the calculation of ea involves specific humidity (SH) and surface pressure (Pr):

$$e_a = \frac{SH \times Pr}{SH \times 0.378 + 0.622}, \quad (2)$$

2.2.3 Correlation-difference method

Another novel correlation-difference metric, proposed by Denissen et al. (2020), evaluates water versus energy-limited conditions using the detrended anomaly of VPD, ET, and SM ~~anomalies.~~ :

$$CorrVPD = Corr(ET, VPD) - Corr(ET, SM), \quad (3)$$

Matlab's corr tool calculates this metric, which uses Kendall's rank correlation (Corr) rather than assuming linear correlations between variables (van Doorn et al., 2018). If CorrVPD > 0, then the grid cell is energy-limited and vegetation anomalies (i.e., ET) correlate more strongly with energy anomalies (i.e., VPD) than with water anomalies (i.e., SM). CorrVPD < 0, in contrast, is water-limited. When CorrVPD ≈ 0, SM is labeled as CSM, indicating that water and energy limit regimes are transitioning.

2.3 Evaluation criteria

The correlation coefficient was applied to evaluate the performance of satellite-based ET from CAMELE, GLASS, PML, and SEBAL and GPP from GOSIF, GLASS, PML, and TL, compared to the eddy covariance observed in-situ ET and GPP. A point-to-pixel evaluation was carried out to evaluate the over- or underestimation of ET and GPP for each land cover type from all 21 flux sites. We summed 8-day ET and GPP changes in grassland, evergreen broadleaf forests, evergreen needleleaf forests, mixed forests, cropland, wetland, and barren land.

The alignment of CSM obtained by different methods was determined using the chi-square test (McHugh, 2013; Hsu and Dirmeyer, 2023a). CROSSTAB in MATLAB was used to perform the chi-square test. SM values were divided into two groups, below and above CSM. In this case, categorical data was tagged as a binary variable of 0 for drier than CSM and 1 for wetter than CSM. If there were significant differences with a 95% confidence level, CSM was different.

2.4 Partial least square regression

Partial least square regression has been widely acknowledged as a viable approach for mitigating collinearity issues among independent variables (Karthikeyan et al., 2020), which is extensively used in quantifying interannual impacts of climate and plant growth variations on water and energy dynamics. Performances of the partial least square regression model were assessed by five-fold cross-validation using the mean absolute percentage error. Here, the dominant factor of precipitation, temperature, incoming shortwave radiation, VPD, ET, GPP, and SM on CorrVPD was identified by the largest variable importance in projection scores.

3 Results

3.1 Consistency of ET and GPP

Figures 2a and b show good agreement between satellite-based products and site observations in most land cover types. Across all sites, correlation coefficients obtained from CAMELE, GLASS, PML, and SEBAL ET were 0.74, 0.65, 0.78, and 0.59, respectively; correlation coefficients obtained from GLASS, TL, GOSIF, and PML GPP were 0.75, 0.71, 0.77, and 0.74, respectively. For ET, the highest correlation coefficient occurred between GLASS and eddy covariance observations in mixed forests (0.96), while the lowest value was between SEBAL and site observations in barren (0.47). For GPP, the highest correlation coefficient was found between TL and site measurements in mixed forests (0.97), while the lowest value was between GLASS and site-based data in barren land (0.32). In general, no single product consistently outperformed ~~the~~ others over all types. Figures 2c and d show the comparison between daily site observations and satellite-based ET and GPP across land cover types. ET had the highest value in evergreen needleleaf forests and was the lowest in barren land, while GPP peaked in evergreen broadleaf forests and was the lowest in wetland. In these land cover types, ET and GPP derived from satellite-based products were also substantially different and varied quite a bit between different products. Especially in evergreen broadleaf forests, ET derived from GLASS (3.37 mm) and CAMELE (3.05 mm) and GPP from GOSIF (7.55 gC m^{-2} day^{-1}) and TL (7.59 gC m^{-2} day^{-1}) were higher than site observations of 1.74 mm and 5.26 gC m^{-2} day^{-1}, respectively. If satellite-based ET and GPP were between ±10% of site-observed values, they were termed as satisfactory; otherwise, they were either overestimated or underestimated. CAMELE, GLASS, PML, and SEBAL ET and GLASS, TL, GOSIF, and PML GPP met satisfied values in 1, 1, 3, 1, 2, 1, 3, and 2 land cover types, respectively. PML ET provided the most satisfactory estimates in evergreen broadleaf forests, cropland, and barren land with an average bias of 1.05%, 1.13%, and 1.34%, respectively; GOSIF GPP provided the most satisfactory estimate in grassland, evergreen needleleaf forests, and mixed forests with an average bias of 4.31%, 9.14%, and 4.29%, respectively. Although discrepancies existed among multi-source remotely sensed products across flux sites, they offered an opportunity to quantify ~~the~~ characteristics of large-scale CSM and examine uncertainties from single-source data.

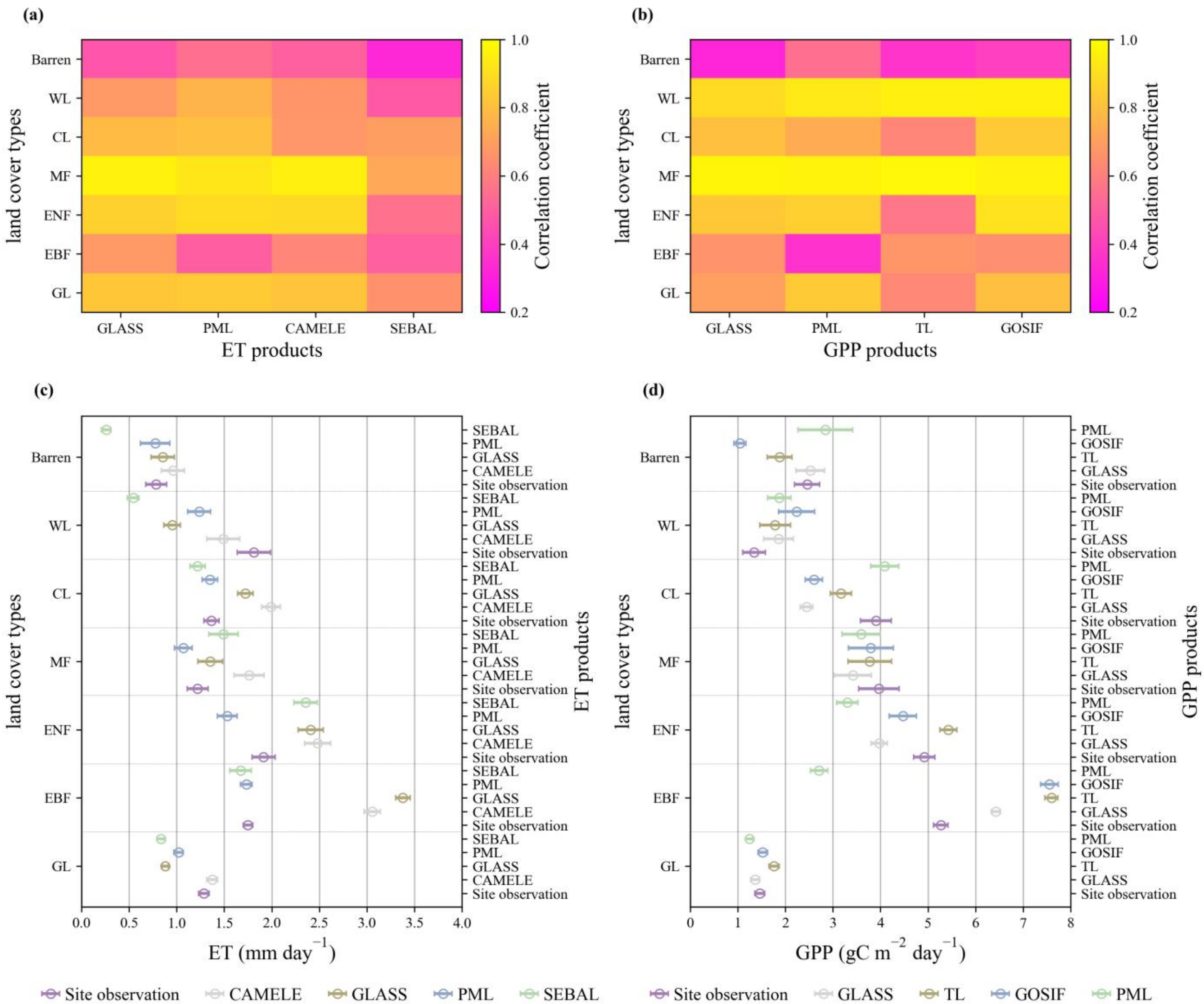

Figure 2: Correlation coefficients between eddy covariance observations and satellite-based (a) ET and (b) GPP products across land cover types, GL: grassland, EBF: evergreen broadleaf forests, ENF: evergreen needleleaf forests, MF: mixed forests, CL: cropland, WL: wetland. Comparison of the daily (c) ET from CAMELE, GLASS, PML, and SEBAL and (d) GPP from GLASS, TL, GOSIF, and PML with site measurements across land cover types. The bars show 95% confidence intervals.

3.2 Consistency of CSM

Variations of SM and EF were depicted in Figure 3 for eight sites. Fitted lines represented controlling mechanisms in various evaporative regimes. Overall, the linear-plus-plateau regression with the lowest BIC outperformed the flat line and the positive slope line in the study period of all eight sites. Specifically, CN-Du2 and Qianyanzhou sites showed a great slope at low SM values with BIC of -80.29 and -98.64, respectively. We also found that grassland CSM in different regions varied greatly.

Ranges of SM across land cover types determined the CSM value. For example, grassland at Xilingela had the lowest CSM of 0.079 m^3/m^3 with SM ranging from 0.06 to 0.20 m^3/m^3; CSM at Damshung, Southwest China, was 0.175 m^3/m^3 with SM ranging from 0.14 to 0.26 m^3/m^3; CSM at CN-Cng in Northeast China was 0.457 m^3/m^3 with high SM ranging from 0.30 to 0.70 m^3/m^3. Moreover, vertical lines of different colors represented CSM derived from CorrVPD using the correlation-difference method and Cov using covariance between VPD and GPP. To explore the performance of both methods on sites and whether they can be used on a large scale, the data applied to both methods was averaged for 8 days, consistent with gridded data with the 8-day time scale. For CN-Du2 and Qianyanzhou sites, only positive or negative Cov and CorrVPD were found. For Damshung, CN-Cng, and Huailai sites, we found more than one SM value where the Cov or CorrVPD was zero. Along with surface soil wetting, there was a change of Cov and CorrVPD from positive to negative at these sites, inconsistent with the transition from water to energy limitation, indicating that CSM was not identifiable. Different from above, Cov had the optimal CSM value that agreed best with the EF-SM-derived CSM at Xilingela and CN-Sw2 sites. Through another technique, CorrVPD was better than Cov at Miyun site. In these sites, Cov and CorrVPD changed from negative (water limit) to positive (energy limit). Therefore, CorrVPD and Cov had the potential to obtain large-scale CSM.

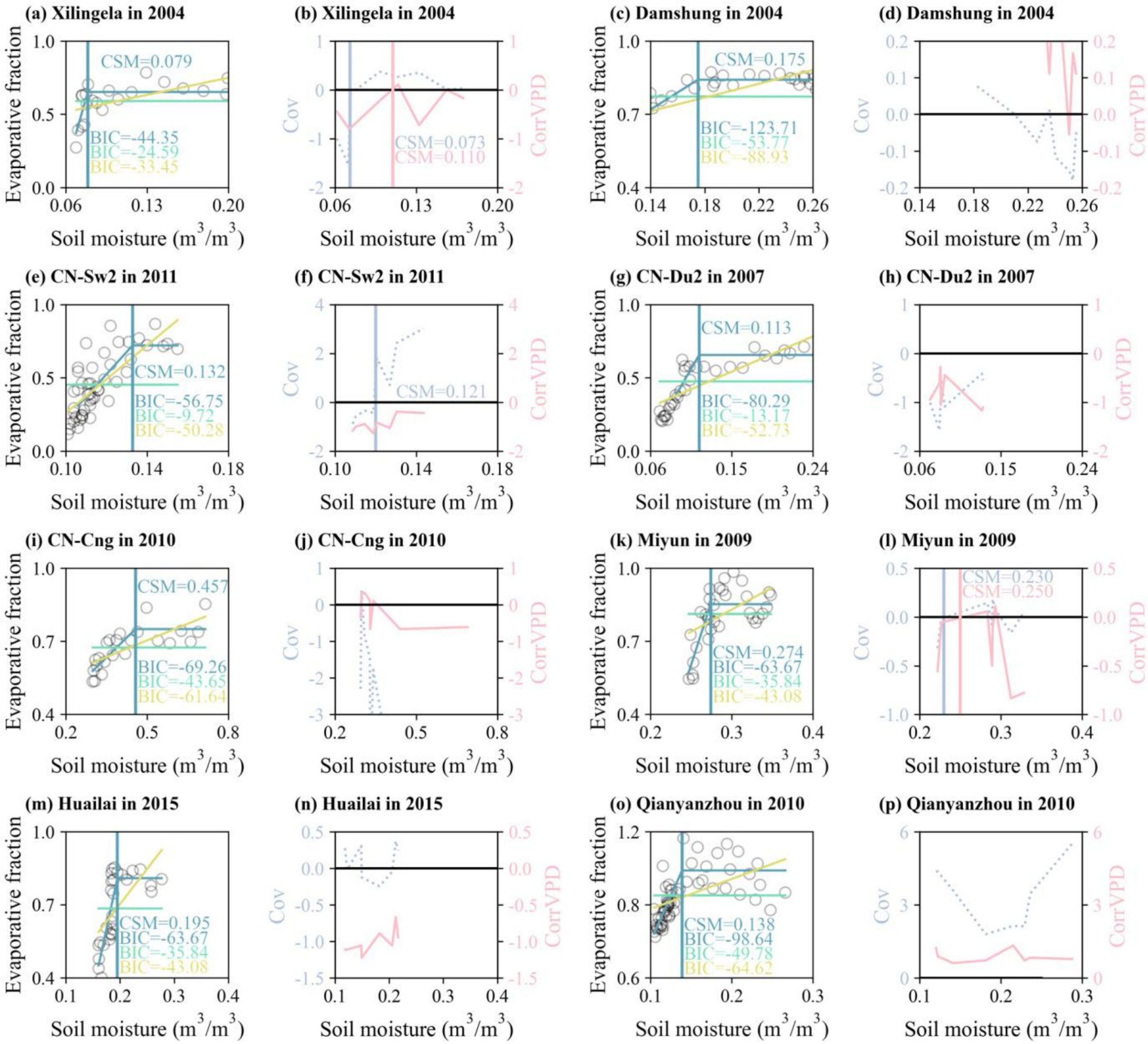

Figure 3: Variations of soil moisture and evaporative fraction at (a) Xilingela in 2004, (c) Damshung in 2004, (e) CN-Sw2 in 2011, (g) CN-Du2 in 2007, (i) CN-Cng in 2010, (k) Miyun in 2009, (m) Huailai in 2015, (o) Qianyanzhou in 2010. Variations of covariance (referred to as Cov) between vapor pressure deficit and gross primary production, and correlation-difference metric (referred to as CorrVPD) at (b) Xilingela in 2004, (d) Damshung in 2004, (f) CN-Sw2 in 2011, (h) CN-Du2 in 2007, (j) CN-Cng in 2010, (l) Miyun in 2009, (n) Huailai in 2015, (p) Qianyanzhou in 2010.

3.3 Spatial pattern of CSM

The number of wet binary bit was used to quantify the agreement among eight ET and GPP-based models at 10 cm soil depth. If CSM was identified, the SM wetter than CSM was represented as 1, and 0 for others. If CSM was not identified within a year, digits of the mode were treated as 0. If CSM was not detected for all 18 years, it was displayed as empty. The intercomparison provided helpful insights to examine the consistency and discrepancy between multi-source ET and GPP products in depicting the spatial distribution of CSM. Figure 4 shows the strong disparity in North and Central China, especially in Inner Mongolian Plateau Region, Songhua River Basin, Yangtze River Basin, and Yellow River Basin. In these regions, the chi-square test showed significant differences among GPP-based models due to their large number of wet binary bits. In addition, TL GPP displayed no CSM value in Northwest China. Note that the SM wetter-than-CSM showed agreement in eastern and southern basins, such as Huaihe River Basin, Liaohe River Basin, Southeastern River Basin, and Pearl River Basin, indicating that ET and GPP-based models were consistent in these basins.

Figure 5 shows the spatial distribution of CSM obtained from covariance between VPD and GOSIF, GLASS, PML, and TL GPP, and correlation-difference metric with Corr between the detrended anomaly of CAMELE, GLASS, PML, SEBAL ET and 10 cm soil depths SM and Corr between the detrended anomaly of ET and VPD. Geographically, they spanned large swaths of land through water-scarce desert regions and lush, rainy forests. Overall, spatial patterns of CSM obtained through ~~the~~ four ET products were consistent with those from ~~the~~ four GPP products, showing a decreasing variation from South to North China. Specifically for water resources subregions, CSM in semi-humid Huaihe River Basin, Haihe River Basin, and Yellow River Basin was about 0.3 m^3/m^3, respectively, and increased to approximately 0.4 m^3/m^3 in Southeastern River Basin and Pearl River Basin. In addition, Table 3 shows the comparison of site CSM from EF-SM and gridded CSM. It was found that gridded CSM values at CN-Cng, Miyun, and Huailai sites were generally consistent with site-based values. Gridded data had spatial continuity, while site observations showed significant differences in CSM even between adjacent sites (e.g., CN-Du2 of 0.113 m^3/m^3 and Miyun of 0.274 m^3/m^3), resulting in inconsistent CSM between satellite and site-based value.

Furthermore, large-scale CSM depended on roots pulling water out of the unsaturated soil matrix (Feldman et al., 2019) and varied across vegetation types and soil textures at four soil layers (Figure 6). With shorter root systems and less vegetation (i.e., barren), areas with low CSM were water-limited. Forest regions displayed a relatively high CSM (e.g., 0.18 m^3/m^3 using PML ET and 10 cm depth SM). As for soil textures, sand covering the large area was further part into content of less than 60%, 60–70%, 70–80%, 80–90%, and higher than 90%. Soil with a majority of clay had a wetter CSM than others (e.g., 0.38 m^3/m^3 using PML ET and 10 cm depth SM) and was to be expected given that clay had a larger negative matric potential compared to coarse soil textures dominated by sand and silt. In summary, fine soils and luxuriant vegetation had wetter CSM. Additionally, a layer-wise CSM analysis was conducted to highlight variations in SM properties for different soil layers. It was evident that there were variations in the CSM behavior across layers with higher SM and CSM at 20 cm soil depth than at other depths. We also found that there was higher CSM than SM at all four layers for grassland and clay, which identified a large range of SM within water-limited regimes. However, for cropland and forests, differences existed in CSM among four ET-based methods, with higher CSM from GLASS and SEBAL than others.

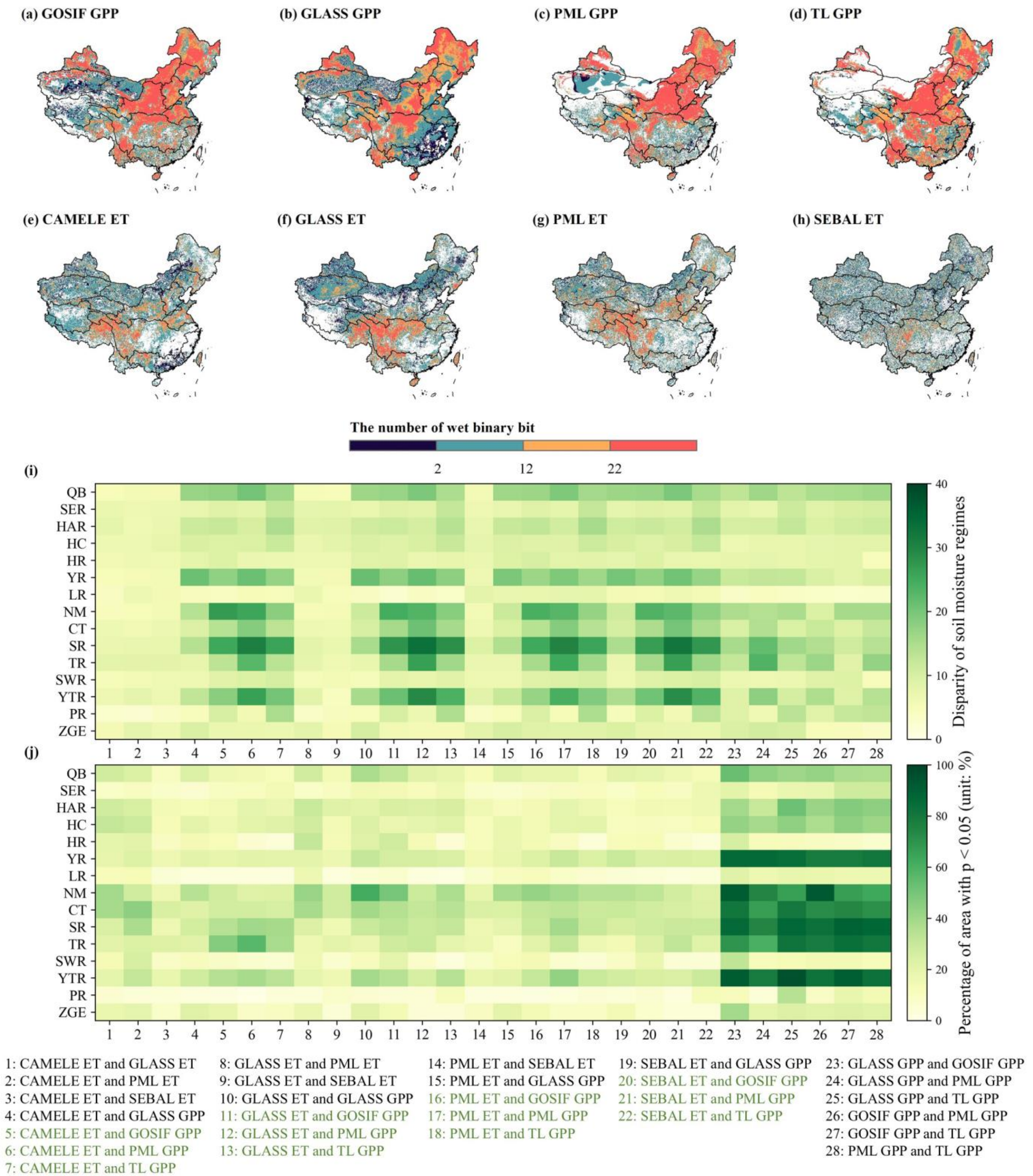
(a) GOSIF GPP
(b) GLASS GPP
(c) PML GPP
(d) TL GPP
(e) CAMELE ET
(f) GLASS ET
(g) PML ET
(h) SEBAL ET
The number of wet binary bit
2
12
22
(i)
QB
SER
HAR
HC
HR
YR
LR
NM
CT
SR
TR
SWR
YTR
PR
ZGE
Disparity of soil moisture regimes
(j)
Percentage of area with p < 0.05 (unit: %)
1: CAMELE ET and GLASS ET
2: CAMELE ET and PML ET
3: CAMELE ET and SEBAL ET
4: CAMELE ET and GLASS GPP
5: CAMELE ET and GOSIF GPP
6: CAMELE ET and PML GPP
7: CAMELE ET and TL GPP
8: GLASS ET and PML ET
9: GLASS ET and SEBAL ET
10: GLASS ET and GLASS GPP
11: GLASS ET and GOSIF GPP
12: GLASS ET and PML GPP
13: GLASS ET and TL GPP
14: PML ET and SEBAL ET
15: PML ET and GLASS GPP
16: PML ET and GOSIF GPP
17: PML ET and PML GPP
18: PML ET and TL GPP
19: SEBAL ET and GLASS GPP
20: SEBAL ET and GOSIF GPP
21: SEBAL ET and PML GPP
22: SEBAL ET and TL GPP
23: GLASS GPP and GOSIF GPP
24: GLASS GPP and PML GPP
25: GLASS GPP and TL GPP
26: GOSIF GPP and PML GPP
27: GOSIF GPP and TL GPP
28: PML GPP and TL GPP

Figure 4: Spatial pattern of number of wet binary bit at 10 cm depth using covariance between vapor pressure deficit (VPD) and gross primary production (GPP) from (a) GOSIF, (b) GLASS, (c) PML, (d) TL. Spatial pattern of number of wet binary bit at 10 cm depth using correlation-difference metric with Kendall's rank correlation (Corr) between detrended anomaly of soil moisture (SM) and evapotranspiration (ET) from (e) CAMELE, (f) GLASS, (g) PML, and (h) SEBAL and Corr between detrended anomaly of VPD and those ET products. (i) Disparity of soil moisture regimes among all methods and (j) the percentage of area with $p < 0.05$. ZGE: Zhungaer Basin, PR: Pearl River Basin, YTR: Yangtze River Basin, SWR: Southwestern River Basin, TR: Tarim Basin, SR: Songhua River Basin, CT: Changthang Region, NM: Inner Mongolian Plateau Region, LR: Liaohe River Basin, YR: Yellow River Basin, HR: Huaihe River Basin, HC: Hexi Corridor Region, HAR: Haihe River Basin, SER: Southeastern River Basin, QB: Qaidam Basin.

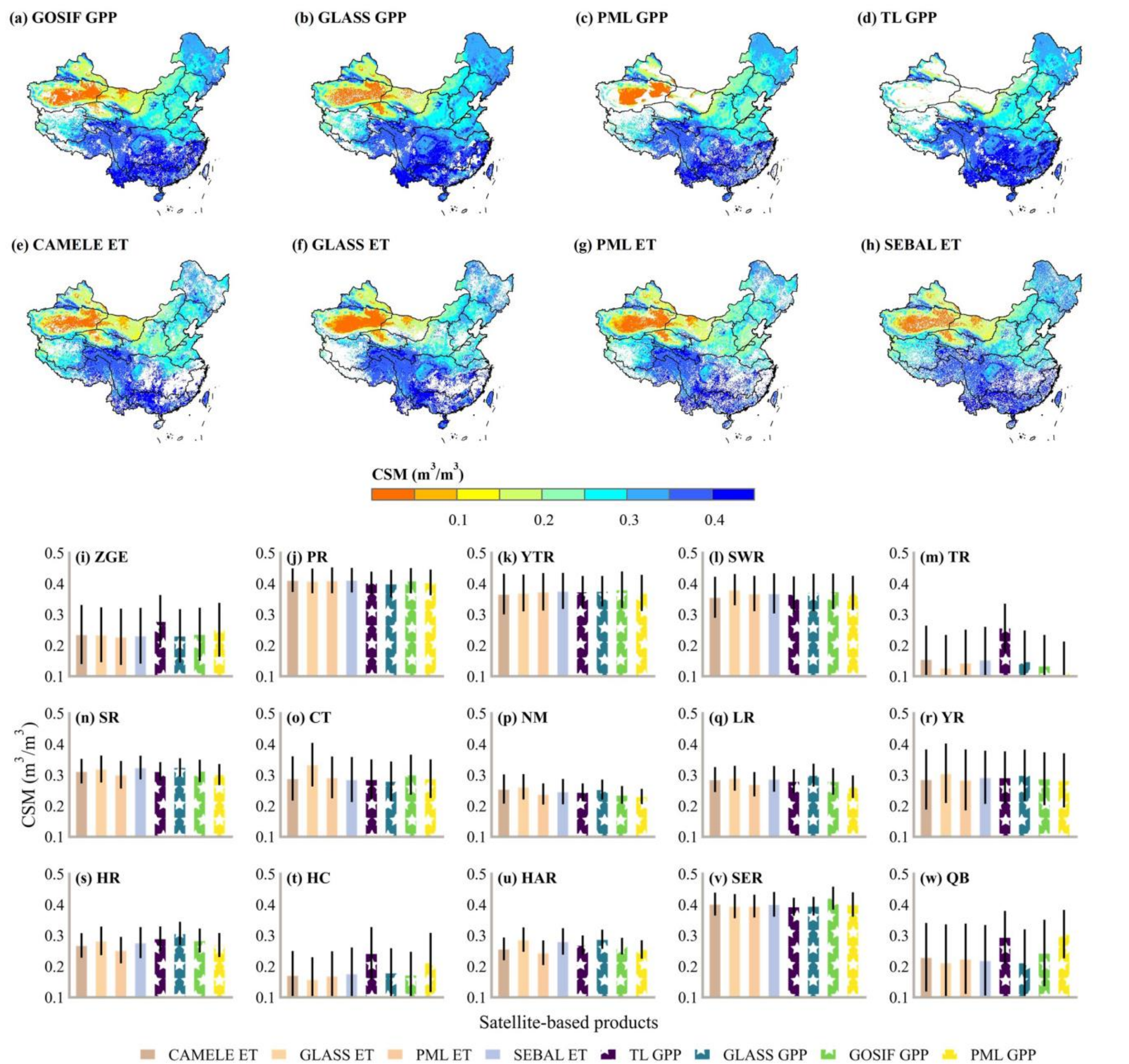

Figure 5: The spatial pattern of critical soil moisture (CSM) at 10 cm depth using covariance between vapor pressure deficit (VPD) and gross primary production (GPP) from (a) GOSIF, (b) GLASS, (c) PML, (d) TL and CSM using correlation-difference metric with Kendall's rank correlation (Corr) between detrended anomaly soil moisture (SM) and evapotranspiration (ET) from (e) CAMELE, (f) GLASS, (g) PML, and (h) SEBAL and Corr between detrended anomaly VPD and those ET products. And (i–w) the basin-average values of ZGE: Zhungaer Basin, PR: Pearl River Basin, YTR: Yangtze River Basin, SWR: Southwestern River Basin, TR: Tarim Basin, SR: Songhua River Basin, CT: Changthang Region, NM: Inner Mongolian Plateau Region, LR: Liaohe River Basin, YR: Yellow River Basin, HR: Huaihe River Basin, HC: Hexi Corridor Region, HAR: Haihe River Basin, SER: Southeastern River Basin, QB: Qaidam Basin.

Table 3: Site CSM from EF-SM and gridded CSM using satellite-based ET and GPP and 10 cm depth SM.

Site	CSM from EF-SM	CSM using GOSIF GPP	CSM using GLASS GPP	CSM using PML GPP	CSM using TL GPP	CSM using CSMELE ET	CSM using GLASS ET	CSM using PML ET	CSM using SEBAL ET
Xilingela	0.079	0.249	0.263	0.250	0.251	0.266	0.303	-	0.296
Damshung	0.175	0.381	0.383	0.383	0.383	-	0.364	0.375	0.403
CN-Sw2	0.132	0.238	0.286	0.218	0.238	-	0.290	0.233	-
CN-Du2	0.113	0.275	0.300	0.252	0.277	0.260	0.299	-	0.292
CN-Cng	0.457	0.339	0.369	0.325	0.341	0.376	0.386	0.292	0.304
Miyun	0.274	0.315	0.336	0.294	0.331	0.304	0.322	0.311	0.316
Huailai	0.195	0.258	0.278	0.228	0.259	0.221	-	-	0.324
Qianyanzhou	0.138	0.452	0.407	0.327	0.418	-	-	-	-

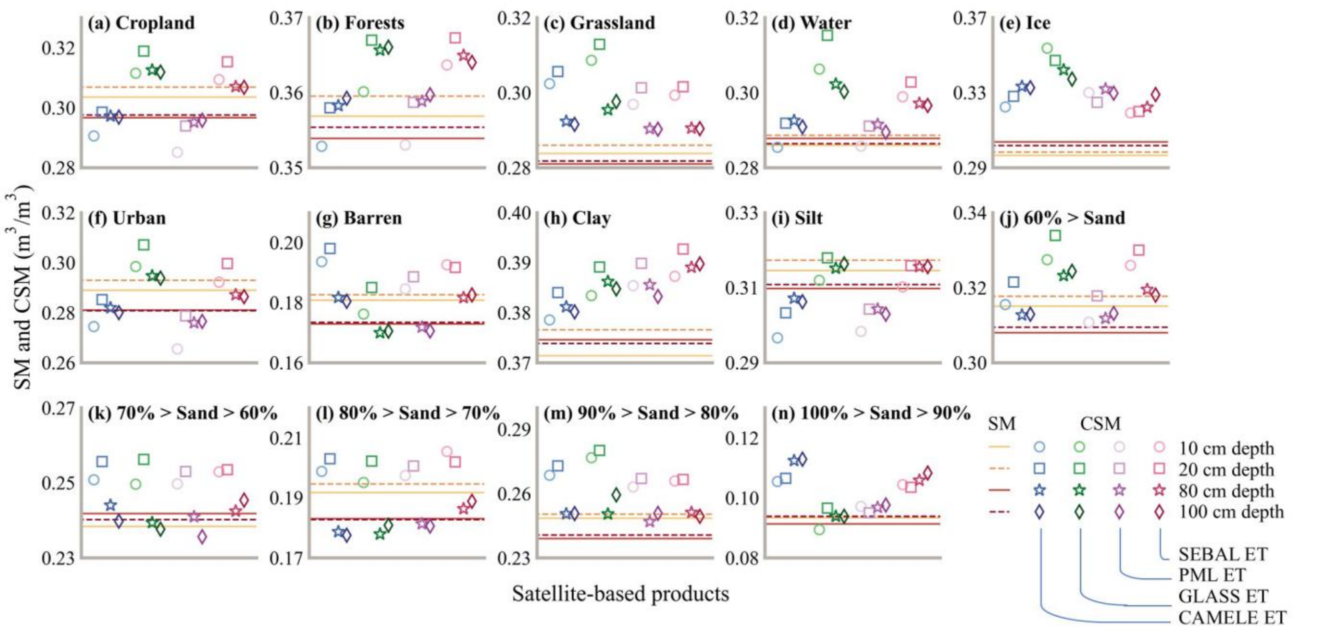

Figure 6: Soil moisture (SM) at 10 cm, 20 cm, 80 cm, and 100 cm soil depths, and critical soil moisture (CSM) derived from CAMELE, GLASS, PML, and SEBAL ET ~~and SM~~ at corresponding soil depths for (a) cropland, (b) forests, (c) grassland, (d) water, (e) ice, (f) urban, (g) barren, soils with a majority of (h) clay, (i) silt, and sand with content (j) less than 60, (k) between 60% and 70%, (l) between 70% and 80%, (m) between 80% and 90%, and (n) higher than 90%.

3.4 Attribution of water and energy limit shifts

We assessed the spatial pattern of multi-annual average CorrVPD at 10 cm soil depth SM over the period 2001–2018 and attributed interannual changes of CorrVPD to hydrological, meteorological, and ecological predictors. GOSIF GPP and PML ET were used for the analysis given the fact that they had the best performance (Section 3.1). As shown in Figure 7a, water-limited regimes were most common in dry and semi-arid areas. Western and northern regions were generally water-limited, while southern regions were energy-limited. The cross-validation using partial least square regression shows that the variance that CorrVPD was explained by precipitation, temperature, incoming shortwave radiation, VPD, ET, GPP, and SM ranged from 73.34% in Yangtze River Basin to 99.95% in Haihe River Basin (Figure 7b).

Variations of dominant factors underlined the relevance of climate and ecosystem variables in inducing shifts in CorrVPD. As shown in Figure 8, blue pixels represented the significant decrease in CorrVPD, indicating increased water stress and correlation between ET and SM. Several typical regions had relatively large areas with significant decreases in CorrVPD, such as Changthang Region (2.62%) and Tarim Basin (3.49%). ET was the most important predictor across 42% of Changthang Region and 24% of Tarim Basin. This confirmed that increasing ET pushed increased water stress in these regions. For Haihe River Basin, decreasing SM contributed to increased water limitation. Contrary to Haihe River Basin, 4.29% of Hexi Corridor Region showed significant increases in CorrVPD; increasing SM contributed to decreased water stress. 16.65% of Songhua River Basin showed significant increases in CorrVPD; decreased water limitation was associated with increasing GPP (greening) in these regions. Moreover, ET and VPD played the most important role in 30% and 24% of Pearl River Basin, respectively; the significant decrease in VPD mitigated drought in these regions.

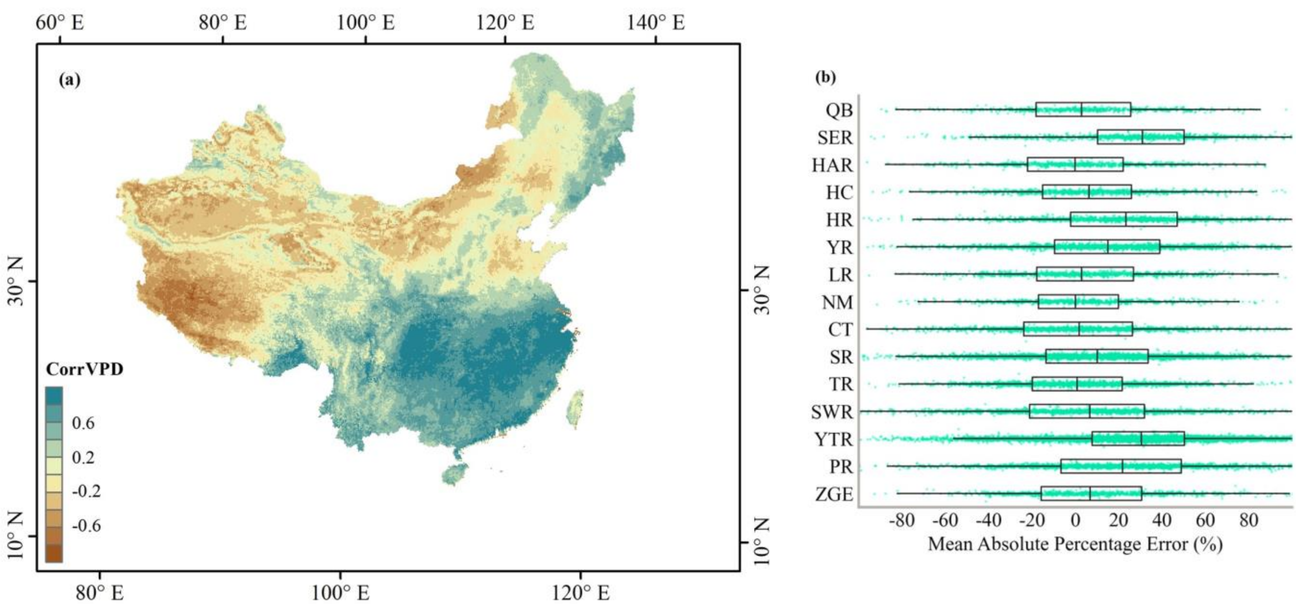

Figure 7: Spatial pattern of (a) CorrVPD derived from PML ET and 10 cm soil depth soil moisture and (b) the mean absolute percentage error based on partial least square regression for CorrVPD estimations. ZGE: Zhungaer Basin, PR: Pearl River Basin,

YTR: Yangtze River Basin, SWR: Southwestern River Basin, TR: Tarim Basin, SR: Songhua River Basin, CT: Changthang Region, NM: Inner Mongolian Plateau Region, LR: Liaohe River Basin, YR: Yellow River Basin, HR: Huaihe River Basin, HC: Hexi Corridor Region, HAR: Haihe River Basin, SER: Southeastern River Basin, QB: Qaidam Basin.

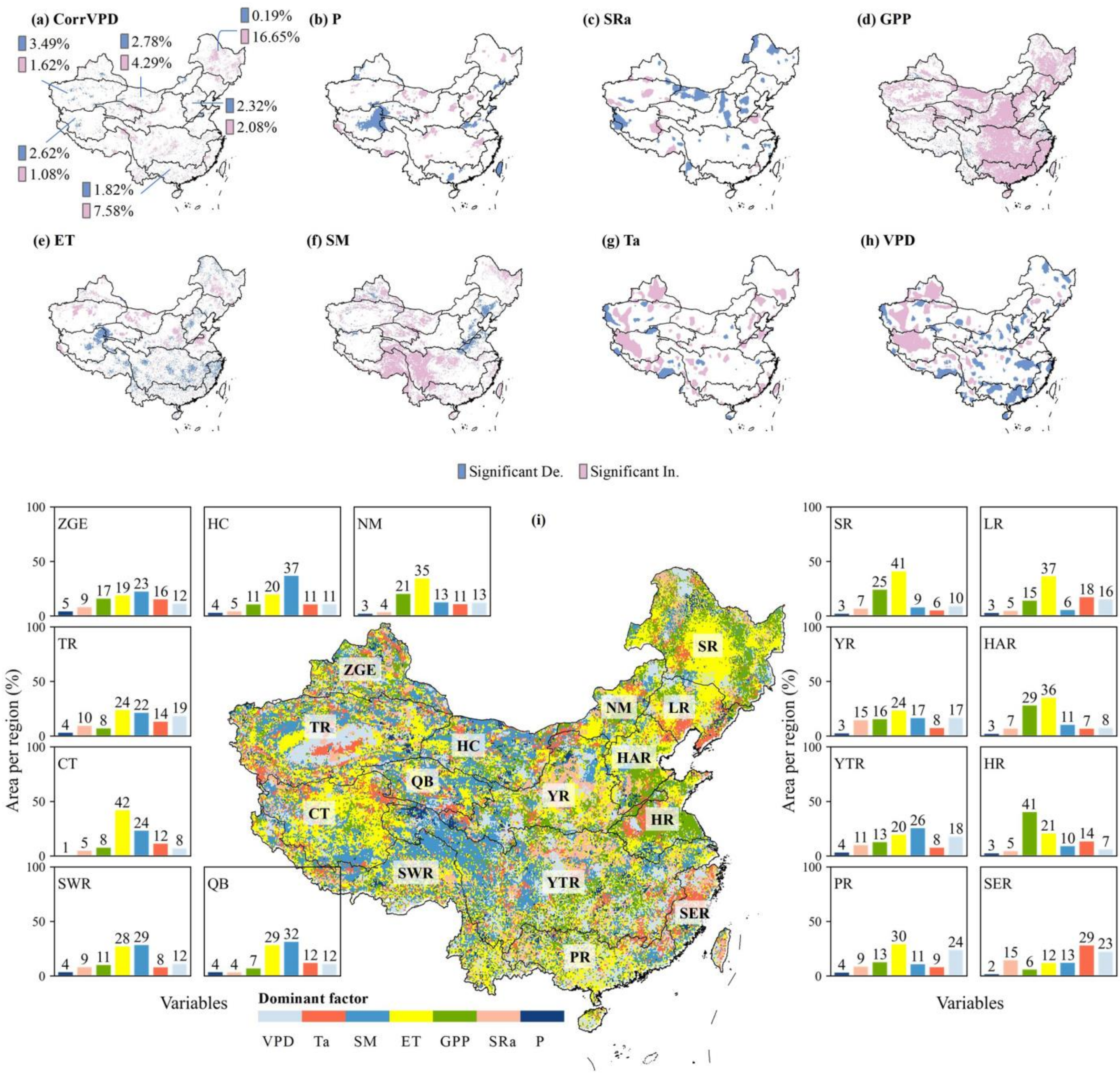

Figure 8: Spatial patterns of significance (p<0.05) of (a) CorrVPD, (b) precipitation (P), (c) incoming shortwave radiation (SRa), (d) GOSIF gross primary production (GPP), (e) PML evapotranspiration (ET), (f) soil moisture (SM), (g) temperature (Ta), and (h) vapor pressure deficit (VPD) during the period of CorrVPD detection using the Mann–Kendall test (Mann, 1945; Kendall, 1948),

"De." Means "decreasing" and "In." means "increasing". (i) Attribution of CorrVPD variations. Colors indicate the variable that best predicts the CorrVPD dynamics. ZGE: Zhungaer Basin, PR: Pearl River Basin, YTR: Yangtze River Basin, SWR: Southwestern River Basin, TR: Tarim Basin, SR: Songhua River Basin, CT: Changthang Region, NM: Inner Mongolian Plateau Region, LR: Liaohe River Basin, YR: Yellow River Basin, HR: Huaihe River Basin, HC: Hexi Corridor Region, HAR: Haihe River Basin, SER: Southeastern River Basin, QB: Qaidam Basin.

4 Discussion

Analysis of spatial patterns of CSM using multi-source satellite-based water and carbon fluxes (Figure 2) derived from different methods (Figure 3) further enables us to effectively reflect variations ~~of~~from energy ~~and~~to water limitation in spatiotemporal continuous grid cells. To address the question of how soil textures and plant features define constraints imposed by water supply and energy availability, there has been a growing focus on CSM from site to continental scales. For instance, Northern California exhibits CSM of 0.15 m^3/m^3 in semi-arid grassland at the site scale (Baldocchi et al., 2004); CSM using satellite-based surface temperature diurnal amplitude in semi-arid grassland of Africa has been reported to be 0.12 m^3/m^3 at the continental scale (Feldman et al. 2019). For specific plants, CSM is around 0.238 m^3/m^3 using PML ET in Inner Mongolian Plateau Region (Figure 5) where grass is abundant. That is in line with the grassland CSM of 0.214 m^3/m^3 from the covariance approach across 195 global sites from the Integrated Carbon Observation System, the AmeriFlux, and the FLUXNET2015 (Fu et al. 2022b). Another study based on the correlation-difference method using SM from the European Space Agency Climate Change Initiative program and ET from the FLUXCOM reported large-scale CSM of around 0.21 m^3/m^3 throughout Europe across all grid cells (Denissen et al., 2020). Researchers also found that plants exhibit a great vertical water uptake range to alleviate the impact of water stress (Gallego-Elvira et al., 2016), with water uptake extending to below 50 cm (Case et al., 2020) or 1–2 m (Tumber-Davila et al., 2022). Low CSM may be attributed to shorter rooting systems in water-limited environments (Konings and Gentine, 2017), while locations with high humidity, such as tropical West Africa and the southern part of Congo Basin (Feldman et al. 2022), exhibit high CSM. Deep-rooted forests can better regulate their response to drought with high CSM among soil layers, which means that root systems of plants play a key part in determining water- and energy-limited regimes and may help understand regional or continental-scale water- and energy-limited regimes that arise from different vegetation and soil conditions. To comprehend the underlying factors driving CSM, it is necessary to do a more comprehensive analysis of climate and ecosystem conditions: CSM detection shows that grassland had a large range of SM within the water-limited regimes (Figure 6), where CSM was higher than average SM, probably because of shallow root systems affected by moisture; therefore, facing decreased CorrVPD, the grassland located in the northwestern arid region is more vulnerable. Further, water-limited regions exhibit great sensitivity in hydrologic cycles to variations in vegetation functioning, climate variability, and catchment physical conditions. Consequently, water-limited vegetation exhibits a higher degree of sensitivity to surface disturbances compared to locations with higher levels of precipitation. In this scenario, the effect of ET is more pronounced, resulting in a decline in energy limitation, such as Tarim Basin. However, this study focusing on a specific time of year may not be enough to explain the critical value that may be shown in the rest of the year. Since CSM values in some grids were not detected by eight products, further research is needed for the CSM that may appear in the rest of the year in different regions. In addition, to compare the performance of multi-source remotely sensed water and carbon fluxes, we unified all data into the 8-day resolution. Therefore, a more refined time scale, such as a one-day scale study, is also needed.

Multiple factors contributed to inherent constraints in identifying different regimes associated with the utilization of multi-source satellite-based ET and GPP. For example, ET and GPP exhibited great uncertainties (Liu et al., 2021) in areas with barren land as indicated in Section 3.1. In eastern and southern regions (Figure 4), where satellite-based methods were more reliable, eight satellite-based SM regimes were in good agreement. Since the CAMELE ET combined PML ET, they showed consistency in cropland and forests with a lower CSM than GLASS and SEBAL (Section 3.3). By considering variations of energy and water limitations in terrestrial ecosystems (Section 3.4), there is potential to improve the water and carbon flux estimation in turn. In addition, SM from ground samplings and gridded sources (Koster et al., 2009) contributed to the uncertainty in characterizing CSM as discussed in Section 3.3. For gridded SM, surface climate shows a significant effect on the upper soil layer SM modeling, while the background aridity leads to low variability of the deeper layer SM (Li, Q. et al., 2022). Besides, external forcings seem to be responsible for a shift towards enhanced land-atmosphere coupling (Zhang et al., 2020). It should be noted that the South-to-North Water Diversion Project and the Pinglu Canal Project in China would result in significant modifications to SM characteristics, which are fundamental components of the concept known as CSM. Water management measures may reduce water stress in grasslands affected by climate change and make southern coastal clay areas more resistant to possible disturbances. Overall, our research could inform large-scale water conservancy projects for better allocation of water supply resources. Future research directions could include the impact of hydraulic projects such as inter-basin water transfers on CSM, the impact of extreme disturbances such as tropical cyclones and wildfires on CSM, and possible changes in CSM.

5 Conclusion

Our main accomplishment is observing and identifying water and energy limit shifts using multi-source satellite-based water and carbon fluxes over China. These shifts show which areas are more likely to be affected by climate change. To do so, we first examined the consistency of ET and GPP derived from the site- and satellite-based grid observations and the consistency of CSM derived from the EF-SM, covariance, and correlation-difference methods. Then, satellite-based CSM from ~~the~~ four ET products, four GPP products, and the latest SM dataset was estimated and evaluated. Based on the spatial pattern of CSM, we further quantified CSM among land cover types, soil textures, and water resource subregions and attributed the dominant factor of water and energy limit shifts.

We discovered that CSM detected by the covariance between VPD and GPP and CSM using the correlation-difference metric using VPD, ET, and SM matches well with CSM using the EF-SM method at the site scale, suggesting that these methods could detect large-scale CSM. Surface water and energy-limited regimes varied among land cover types, soil textures, and water resources subregions. Soil textures of clay and land cover types of grassland had a large range of SM within water-limited regimes. VPD was the most important predictor across 24% of Pearl River Basin and 19% of Tarim Basin. However, unlike the declining VPD in Pearl River Basin, the increasing VPD aggravated the water stress in Tarim Basin, especially for the more fragile grassland in these areas. 18 years of SM data were quite typical of the long-term climatology of continental wetness. Applying our analysis to CSM has considerable significance in the evaluation of global climate change impacts on regional terrestrial ecosystems over extended periods.

Data availability

National Tibetan Plateau Data Center (TPDC) offers eight flux sites, consisting of four locations inside the Hexi Corridor Region (Huazhaizi, Dashalong, Luodi, and Arou) and four cropland sites within the Haihe River Basin (Guantao, Huailai, Miyun, and Daxing) with half-hour records (http://data.tpdc.ac.cn/). ChinaFlux offers data from Damshung, Xilingela, Xishuangbanna, Dinghushan, Qianyanzhou, Changbaishan, Yucheng, Haibei1, and Haibei2 flux sites (http://www.chinaflux.org/). Fluxnet includes four grassland sites, CN-Sw2, CN-Du2, CN-Du3, and CN-Cng with daily records, which are available at https://fluxnet.org/data/download-data/. PML provides ET and GPP on TPDC website. GLASS ET and GPP are provided by http://glass.umd.edu/. CAMELE ET is available at Zenodo: https://zenodo.org/record/6283239/. SEBAL ET is publicly accessible from the Zenodo repository at https://doi.org/10.5281/zenodo.4243988 and https://doi.org/10.5281/zenodo.4896147/. TL GPP is available at https://doi.org/10.5061/dryad.dfn2z352k/. GOSIF GPP is obtained from https://globalecology.unh.edu/.Gridded soil moisture and meteorological data is available in TPDC. Land cover types and soil textures were contributed by Data Center for Resources and Environmental Sciences, Chinese Academy of Sciences (http://www.resdc.cn/).

Author contributions

Yi Liu: investigation, methodology, formal analysis, conceptualization, writing (original draft and review and editing); Jingfeng Xiao: supervision, writing (review and editing); Xing Li: writing (review and editing); Yue Li: writing (review and editing).

Competing interests

The contact author has declared that none of the authors has any competing interests.

Financial support

Y. Liu acknowledges support from Guangxi Natural Science Foundation under Grant No. 2024GXNSFBA010180 and Guangxi University.

References

Akbar, R., Gianotti, D. J. S., McColl, K. A., Haghighi, E.¸ Salvucci, G. D., and Entekhabi, D.: Estimation of Landscape Soil Water Losses from Satellite Observations of Soil Moisture, Journal of Hydrometeorology, 19, 871–889. https://doi.org/10.1175/JHM-D-17-0200.1, 2018.

Baldocchi, D. D., Xu, L. K., and Kiang, N.: How plant functional-type, weather, seasonal drought, and soil physical properties alter water and energy fluxes of an oak-grass savanna and an annual grassland, Agricultural and Forest Meteorology, 123, 13–39, https://doi.org/10.1016/j.agrformet.2003.11.006, 2004.

Bi, W., He, W., Zhou, Y., Ju, W., Liu, Y., Liu, Y., Zhang, X., Wei, X., and Cheng, N.: A global 0.05 degrees dataset for gross primary production of sunlit and shaded vegetation canopies from 1992 to 2020, Scientific Data, 9, 213 https://doi.org/10.1038/s41597-022-01309-2, 2022.

Bolton, D.: The computation of equivalent potential temperature, Mon. Weather Rev., 108, 1046–1053, https://doi.org/10.1175/2008MWR2593.1, 1980.

Case, M. F., Nippert, J. B., Holdo, R. M., and Staver, A. C.: Root-niche separation between savanna trees and grasses is greater on sandier soils, Journal of Ecology, 108, 2298–2308, https://doi.org/10.1111/1365-2745.13475, 2020.

Cheng, M., Jiao, X., Li, B., Yu, X., Shao, M., and Jin, X.: Long time series of daily evapotranspiration in China based on the SEBAL model and multisource images and validation, Earth System Science Data, 13, 3995–4017, https://doi.org/10.5194/essd-13-3995-2021, 2021.

Denissen, J. M. C., Teuling, A. J., Reichstein, M., and Orth, R.: Critical Soil Moisture Derived from Satellite Observations Over Europe, Journal of Geophysical Research-Atmospheres, 125, e2019JD031672, https://doi.org/10.1029/2019JD031672, 2020.

Dirmeyer, P. A., Jin, Y., Singh, B., and Yan, X.: Trends in Land-Atmosphere Interactions from CMIP5 Simulations, Journal of Hydrometeorology, 14, 829–849, https://doi.org/10.1175/JHM-D-12-0107.1, 2013.

Dong, J., Akbar, R., Feldman, A. F., Gianotti, D. S., and Entekhabi, D.: Land Surfaces at the Tipping-Point for Water and Energy Balance Coupling, Water Resources Research, 59, e2022WR032472, https://doi.org/10.1029/2022wr032472, 2023.

Duan, S. Q., Findell, K. I., and Fueglistaler, S. A.: Coherent Mechanistic Patterns of Tropical Land Hydroclimate Changes, Geophysical Research Letters, 50, e2022GL102285, https://doi.org/10.1029/2022gl102285, 2023.

Feldman, A. F., Gianotti, D. J. S., Trigo, I. F., Salvucci, G. D., and Entekhabi, D.: Satellite-Based Assessment of Land Surface Energy Partitioning-Soil Moisture Relationships and Effects of Confounding Variables, Water Resources Research, 55, 10657–10677, https://doi.org/10.1029/2019WR025874, 2019.

Feldman, A. F., Short Gianotti, D. J., Trigo, I. F., Salvucci, G. D., and Entekhabi, D.: Observed Landscape Responsiveness to Climate Forcing, Water Resources Research, 58, e2021WR030316, https://doi.org/10.1029/2021WR030316, 2022.

Fu, Z., Ciais, P., Wigneron, J. P., Gentine, P., Feldman, A. F., Makowski, D., Viovy, N., Kemanian, A. R., Goll, D. S., Stoy, P. C., Prentice, I. C., Yakir, D., Liu, L., Ma, H., Li, X., Huang, Y., Yu, K., Zhu, P., Li, X., Zhu, Z., Lian, J., and Smith, W. K.:

Global critical soil moisture thresholds of plant water stress, Nature communications, 15, 4826–4826, https://doi.org/10.1038/s41467-024-49244-7, 2024.

Fu, Z., Ciais, P., Feldman, A. F., Gentine, P., Makowski, D., Prentice, I. C., Stoy, P. C., Bastos, A., and Wigneron, J.-P.: Critical soil moisture thresholds of plant water stress in terrestrial ecosystems, Science advances, 8, eabq7827, https://doi.org/10.1126/sciadv.abq7827, 2022b.

Fu, Z., Ciais, P., Makowski, D., Bastos, A., Stoy, P. C., Ibrom, A., Knohl, A., Migliavacca, M., Cuntz, M., Sigut, L., Peichl, M., Loustau, D., El-Madany, T. S., Buchmann, N., Gharun, M., Janssens, I., Markwitz, C., Gruenwald, T., Rebmann, C., Molder, M., Varlagin, A., Mammarella, I., Kolari, P., Bernhofer, C., Heliasz, M., Vincke, C., Pitacco, A., Cremonese, E., Foltynova, L., and Wigneron, J.-P.: Uncovering the critical soil moisture thresholds of plant water stress for European ecosystems, Global Change Biology, 28, 2111–2123, https://doi.org/10.1111/gcb.16050, 2022a.

Gallego-Elvira, B., Taylor, C. M., Harris, P. P., Ghent, D., Veal, K. L., and Folwell, S. S.: Global observational diagnosis of soil moisture control on the land surface energy balance, Geophysical Research Letters, 43, 2623–2631, https://doi.org/10.1002/2016GL068178, 2016.

Gentine, P., Green, J. K., Guerin, M., Humphrey, V., Seneviratne, S. I., Zhang, Y., and Zhou, S.: Coupling between the terrestrial carbon and water cycles-a review, Environmental Research Letters, 14, 083003, https://doi.org/10.1088/1748-9326/ab22d6, 2019.

Good, S. P., Noone, D., and Bowen, G.: Hydrologic connectivity constrains partitioning of global terrestrial water fluxes, Science, 349, 175–177, https://doi.org/10.1126/science.aaa5931, 2015.

Grossiord, C., Buckley, T. N., Cernusak, L. A., Novick, K. A., Poulter, B., Siegwolf, R. T. W., Sperry, J. S., and McDowell, N. G.: Plant responses to rising vapor pressure deficit, New Phytologist, 226, 1550–1566, https://doi.org/10.1111/nph.16485, 2020.

Haghighi, E., Gianotti, D. J. S., Akbar, R., Salvucci, G. D., and Entekhabi, D.: Soil and Atmospheric Controls on the Land Surface Energy Balance: A Generalized Framework for Distinguishing Moisture-Limited and Energy-Limited Evaporation Regimes, Water Resources Research, 54, 1831–1851, https://doi.org/10.1002/2017WR021729, 2018.

He, J., Yang, K., Tang, W., Lu, H., Qin, J., Chen, Y., and Li, X.: The first high-resolution meteorological forcing dataset for land process studies over China, Scientific Data, 7, 25, https://doi.org/10.1038/s41597-020-0369-y, 2020.

He, S., Zhang, Y., Ma, N., Tian, J., Kong, D., and Liu, C.: A daily and 500 m coupled evapotranspiration and gross primary production product across China during 2000-2020, Earth System Science Data, 14, 5463–5488, https://doi.org/10.5194/essd-14-5463-2022, 2022.

Herman, M. R., Nejadhashemi, A. P., Abouali, M., Hernandez-Suarez, J. S., Daneshvar, F., Zhang, Z., Anderson, M. C., Sadeghi, A. M., Hain, C. R., and Sharifi, A.: Evaluating the role of evapotranspiration remote sensing data in improving hydrological modeling predictability, Journal of Hydrology, 556, 39–49, https://doi.org/10.1016/j.jhydrol.2017.11.009, 2018.

Homaee, A., Feddes, R. A., and Dirksen, C.: Simulation of root water uptake II. Non-uniform transient water stress using different reduction functions, Agricultural Water Management, 57, 111–126, https://doi.org/10.1016/S0378-3774(02)00071-9, 2002.

Hsu, H., and Dirmeyer, P. A.: Soil moisture-evaporation coupling shifts into new gears under increasing CO2, Nature Communications, 14, 1162, https://doi.org/10.1038/s41467-023-36794-5, 2023a.

Hsu, H., and Dirmeyer, P. A.: Uncertainty in Projected Critical Soil Moisture Values in CMIP6 Affects the Interpretation of a More Moisture-Limited World, Earths Future, 11, e2023EF003511, https://doi.org/10.1029/2023ef003511, 2023b.

Karthikeyan, L., Chawla, I., Mishra, A. K.: A review of remote sensing applications in agriculture for food security: Crop growth and yield, irrigation, and crop losses, Journal of Hydrology, 586: 124905, https://doi.org/10.1016/j.jhydrol.2020.124905, 2020.

Kendall, M. G.: Rank Correlation Methods, Hafner 160 pp., https://doi.org/10.1017/S0020268100013019, 1948.

Konings, A. G., and Gentine, P.: Global variations in ecosystem-scale isohydricity, Global Change Biology, 23, 891–905, https://doi.org/10.1111/gcb.13389. 2017.

Koster, R. D., Guo, Z., Yang, R., Dirmeyer, P. A., Mitchell, K., and Puma, M. J.: On the Nature of Soil Moisture in Land Surface Models, Journal of Climate, 22, 4322–4335, https://doi.org/10.1175/2009JCLI2832.1, 2009.

Laio, F., Porporato, A., Ridolfi, L., and Rodriguez-Iturbe, I.: Plants in water-controlled ecosystems: active role in hydrologic processes and response to water stress - II. Probabilistic soil moisture dynamics, Advances in Water Resources, 24, 707–723, https://doi.org/10.1016/S0309-1708(01)00005-7, 2001.

Li, C., Yang, H., Yang, W., Liu, Z., Jia, Y., Li, S., and Yang, D.: CAMELE: Collocation-Analyzed Multi-source Ensembled Land Evapotranspiration Data, Earth Syst. Sci. Data Discuss, [preprint], https://doi.org/10.5194/essd-2021-456, 2022.

Li, F., Xiao, J., Chen, J., Ballantyne, A., Jin, K., Li, B., Abraha, M., and John, R.: Global water use efficiency saturation due to increased vapor pressure deficit, Science, 381, 672–677, https://doi.org/10.1126/science.adf5041, 2023.

Li, Q., Shi, G., Shangguan, W., Nourani, V., Li, J., Li, L., Huang, F., Zhang, Y., Wang, C., Wang, D., Qiu, J., Lu, X., and Dai, Y.: A 1 km daily soil moisture dataset over China using in situ measurement and machine learning, Earth System Science Data, 14, 5267–5286, https://doi.org/10.5194/essd-14-5267-2022, 2022.

Li, X., and Xiao, J.: Mapping Photosynthesis Solely from Solar-Induced Chlorophyll Fluorescence: A Global, Fine-Resolution Dataset of Gross Primary Production Derived from OCO-2, Remote Sensing, 11, 2563, https://doi.org/10.3390/rs11212563, 2019.

Li, X., Ryu, Y., Xiao, J., Dechant, B., Liu, J., Li, B., Jeong, S., and Gentine, P.: New-generation geostationary satellite reveals widespread midday depression in dryland photosynthesis during 2020 western US heatwave, Science Advances, 9, eadi0775, https://doi.org/10.1126/sciadv.adi0775, 2023.

Liu, W., Mo, X., Liu, S., Lin, Z., and Lv, C.: Attributing the changes of grass growth, water consumed and water use efficiency over the Tibetan Plateau, Journal of Hydrology, 598, 126464, https://doi.org/10.1016/j.jhydrol.2021.126464, 2021.

Liu, Y., Mo, X., Hu, S., Chen, X., and Liu, S.: Attribution analyses of evapotranspiration and gross primary productivity changes in Ziya-Daqing basins, China during 2001–2015, Theoretical and Applied Climatology, 139, 1175–1189, https://doi.org/10.1007/s00704-019-03004-6, 2020.

Liu, Y. Y., Dorigo, W. A., Parinussa, R. M., de Jeu, R. A. M., Wagner, W., McCabe, M. F., Evans, J. P., and van Dijk, A. I. J. M.: Trend-preserving blending of passive and active microwave soil moisture retrievals, Remote Sensing of Environment, 123, 280–297, https://doi.org/10.1016/j.rse.2012.03.014, 2012.

Mann, H. B.: Non-parametric test against trend, Econometrica, 13, 245–259, https://doi.org/10.2307/1907187, 1945.

McHugh, M. L: The Chi-square test of independence, Biochem. Med., 23, 143–149, https://doi.org/10.11613/bm.2013.018, 2013.

Nash, J.E., Sutcliffe, J.V.: River flow forecasting through conceptual models part I – a discussion of principles, Journal of Hydrology, 10, 282–290, https://doi.org/10.1016/0022-1694(70)90255-6, 1970.

Porporato, A., D'Odorico, P., Laio, F., Ridolfi, L., and Rodriguez-Iturbe, I.: Ecohydrology of water-controlled ecosystems, Advances in Water Resources, 25, 1335–1348, https://doi.org/10.1016/S0309-1708(02)00058-1, 2002.

Rodriguez-Iturbe, I.: Ecohydrology: A hydrologic perspective of climate-soil-vegetation dynamics, Water Resources Research, 36, 3–9, https://doi.org/10.1029/1999WR900210, 2000.

Schwarz, G.: Estimating the Dimension of a Model. The Annals of Statistics, 6, 461–464, https://doi.org/10.1214/aos/1176344136, 1978.

Schwingshackl, C., Hirschi, M., and Seneviratne, S. I.: Quantifying Spatiotemporal Variations of Soil Moisture Control on Surface Energy Balance and Near-Surface Air Temperature, Journal of Climate, 30, 7105–7124, https://doi.org/10.1175/JCLI-D-16-0727.1, 2017.

Seneviratne, S. I., Corti, T., Davin, E. L., Hirschi, M., Jaeger, E. B., Lehner, I., Orlowsky, B., and Teuling, A. J.: Investigating soil moisture-climate interactions in a changing climate: A review, Earth-Science Reviews, 99, 125–161, https://doi.org/10.1016/j.earscirev.2010.02.004, 2010.

Seneviratne, S. I., Luethi, D., Litschi, M., and Schaer, C.: Land-atmosphere coupling and climate change in Europe, Nature, 443, 205–209, https://doi.org/10.1038/nature05095, 2006.

Teuling, A. J., Uijlenhoet, R., van den Hurk, B., and Seneviratne, S. I.: Parameter Sensitivity in LSMs: An Analysis Using Stochastic Soil Moisture Models and ELDAS Soil Parameters, Journal of Hydrometeorology, 10, 751–765, https://doi.org/10.1175/2008JHM1033.1, 2009.

Tumber-Davila, S. J., Schenk, H. J., Du, E., and Jackson, R. B.: Plant sizes and shapes above and belowground and their interactions with climate, New Phytologist, 235, 1032–1056, https://doi.org/10.1111/nph.18031, 2022.

van Doorn, J., Ly, A., Marsman, M., and Wagenmakers, E.-J.: Bayesian Inference for Kendall's Rank Correlation Coefficient, American Statistician, 72, 303–308, https://doi.org/10.1080/00031305.2016.1264998, 2018.

Xiao, J.: Satellite evidence for significant biophysical consequences of the "Grain for Green" Program on the Loess Plateau in China, Journal of Geophysical Research-Biogeosciences, 119, 2261–2275, https://doi.org/10.1002/2014JG002820, 2014.

Yang, K., He, J., Tang, W., Qin, J., and Cheng, C. C. K.: On downward shortwave and longwave radiations over high altitude regions: Observation and modeling in the Tibetan Plateau, Agricultural and Forest Meteorology, 150, 38–46, https://doi.org/10.1016/j.agrformet.2009.08.004, 2010.

Yao, Y., Liang, S., Cheng, J., Liu, S., Fisher, J. B., Zhang, X., Jia, K., Zhao, X., Qing, Q., Zhao, B., Han, S., Zhou, G., Zhou, G., Li, Y., and Zhao, S.: MODIS-driven estimation of terrestrial latent heat flux in China based on a modified Priestley-Taylor algorithm, Agricultural and Forest Meteorology, 171, 187–202, https://doi.org/10.1016/j.agrformet.2012.11.016, 2013.

Yao, Y., Liang, S., Li, X., Hong, Y., Fisher, J. B., Zhang, N., Chen, J., Cheng, J., Zhao, S., Zhang, X., Jiang, B., Sun, L., Jia, K., Wang, K., Chen, Y., Mu, Q., and Feng, F.: Bayesian multimodel estimation of global terrestrial latent heat flux from eddy covariance, meteorological, and satellite observations, Journal of Geophysical Research-Atmospheres, 119, 4521–4545, https://doi.org/10.1002/2013JD020864, 2014.

Yuan, W., Cai, W., Xia, J., Chen, J., Liu, S., Dong, W., Merbold, L., Law, B., Arain, A., Beringer, J., Bernhofer, C., Black, A., Blanken, P. D., Cescatti, A., Chen, Y., Francois, L., Gianelle, D., Janssens, I. A., Jung, M., Kato, T., Kiely, G., Liu, D., Marcolla, B., Montagnani, L., Raschi, A., Roupsard, O., Varlagin, A., and Wohlfahrt, G.: Global comparison of light use efficiency models for simulating terrestrial vegetation gross primary production based on the La Thuile database, Agricultural and Forest Meteorology, 192, 108–120, https://doi.org/10.1016/j.agrformet.2014.03.007, 2014.

Yuan, W., Liu, S., Zhou, G., Zhou, G., Tieszen, L. L., Baldocchi, D., Bernhofer, C., Gholz, H., Goldstein, A. H., Goulden, M. L., Hollinger, D. Y., Hu, Y., Law, B. E., Stoy, P. C., Vesala, T., Wofsy, S. C., and AmeriFlux, C.: Deriving a light use efficiency model from eddy covariance flux data for predicting daily gross primary production across biomes, Agricultural and Forest Meteorology, 143, 189–207, https://doi.org/10.1016/j.agrformet.2006.12.001, 2007.

Zhang, P., Jeong, J.-H., Yoon, J.-H., Kim, H., Wang, S. Y. S., Linderholm, H. W., Fang, K., Wu, X., and Chen, D.: Abrupt shift to hotter and drier climate over inner East Asia beyond the tipping point, Science, 370, 1095-+, https://doi.org/10.1126/science.abb3368, 2020.

Zhang, Y., Kong, D., Gan, R., Chiew, F. H. S., McVicar, T. R., Zhang, Q., and Yang, Y.: Coupled estimation of 500 m and 8-day resolution global evapotranspiration and gross primary production in 2002–2017, Remote Sensing of Environment, 222, 165–182, https://doi.org/10.1016/j.rse.2018.12.031, 2019.

Zhu, W., Wang, Y., and Jia, S.: A remote sensing-based method for daily evapotranspiration mapping and partitioning in a poorly gauged basin with arid ecosystems in the Qinghai-Tibet Plateau, Journal of Hydrology, 616, 128807, https://doi.org/10.1016/j.jhydrol.2022.128807, 2023.